

# Improved interfacial electronic contacts powering high sulfur utilization in all-solid-state lithium–sulfur batteries

Li-Peng Hou<sup>a,1</sup>, Hong Yuan<sup>b,1</sup>, Chen-Zi Zhao<sup>a,1</sup>, Lei Xu<sup>b</sup>, Gao-Long Zhu<sup>a,d</sup>, Hao-Xiong Nan<sup>a,c</sup>, Xin-Bing Cheng<sup>a</sup>, Quan-Bing Liu<sup>c</sup>, Chuan-Xin He<sup>d</sup>, Jia-Qi Huang<sup>b,\*\*</sup>, Qiang Zhang<sup>a,\*</sup>

<sup>a</sup> Beijing Key Laboratory of Green Chemical Reaction Engineering and Technology, Department of Chemical Engineering, Tsinghua University, Beijing, 100084, China

<sup>b</sup> Advanced Research Institute of Multidisciplinary Science, Beijing Institute of Technology, Beijing, 100081, China

<sup>c</sup> School of Chemical Engineering and Light Industry, Guangdong University of Technology, Guangzhou, 510006, China

<sup>d</sup> Shenzhen Key Laboratory of Functional Polymer, College of Chemistry and Chemical Engineering, Shenzhen University, Shenzhen, 518000, China

## ARTICLE INFO

### Keywords:

All-solid-state batteries  
Lithium–sulfur batteries  
Sulfur utilization  
Nanostructured cathode  
Reaction kinetics

## ABSTRACT

All-solid-state lithium–sulfur batteries (ASSLSBs) afford a novel avenue for next-generation high energy density lithium–sulfur batteries due to the alleviated potential safety hazards. However, ASSLSBs suffer from high interfacial impedance and poor kinetics of electrochemical reactions. Herein, we probed the interfacial electron transfer between active sulfur and conductive carbon in a working cell. The co-axial carbon nanotube@sulfur composite with more robust electron contacts enables fast electron transportation and reduced interfacial charge transfer impedance, leading to a high sulfur utilization and excellent electrochemical performance. An initial discharge capacity of 1138.7 mAh g<sup>-1</sup> at 0.21 mA cm<sup>-2</sup> (0.1C) with a capacity retention of 87.7% after 200 cycles is achieved at a sulfur loading of 1.3 mg cm<sup>-2</sup>. Moreover, the cathode with superior and uniform electronic contacts delivers better rate capability and a higher discharge specific capacity at a high sulfur loading ranging from 3.8 to 5.9 mg cm<sup>-2</sup>. This work verifies the significance of 3D interconnected electronic pathways in the sulfur cathode for high performance ASSLSBs.

## 1. Introduction

Lithium–sulfur (Li–S) batteries with a very high theoretical energy density of 2600 Wh kg<sup>-1</sup> are strongly considered as one of the most promising candidates for next-generation energy storage systems [1]. However, complicated conversion mechanism of sulfur electrochemistry based on liquid electrolyte induces the generation of soluble polysulfide intermediates. The diffusion and shuttle of polysulfides between anode and cathode induces low Coulombic efficiency and fast capacity degradation. Furthermore, inevitable lithium dendrite growth resulted from the applications of metallic lithium metal anode also causes the potential safety hazards for a working battery [2,3].

Recently, all-solid-state Li–S batteries (ASSLSBs) have attracted strong attentions due to the possibility of achieving higher energy densities [4–6]. On one hand, the entirely different electrochemical processes where sulfur electrochemistry doesn't undergo the polysulfide formation, completely avoid the shuttle effect in solid state batteries [7,

8]. On the other hand, the intrinsic rigidity and nonflammability of solid-state electrolyte are capable of limiting lithium dendrite growth and reducing fire risk, significantly improving the battery safety [9–12]. Although recent breakthroughs in achieving high ionic conductivity have been gained for emerging solid electrolytes, especially for sulfide solid electrolytes [13], issues such as poor ion/electron transport between solid-solid interfaces and resultant sluggish reaction kinetics and low sulfur utilization, still require to be addressed for ASSLSBs [14,15].

Generally, sulfur is an electronic and ionic insulator [16], the electrochemical reaction of sulfur strongly relies on the electron and ion transport through the triple-phase interfaces between sulfur, solid electrolyte, and conductive additives. Owing to lacking of the infiltration and wetting of liquid electrolyte enabling smooth lithium ion transport in a liquid-electrolyte battery, lithium ion transfer at electrode/electrolyte interface (that is the point-point contact between solid and solid) has been generally considered as one of the main limitations for sulfur electrochemical conversion in a solid-state battery [17,18]. Therefore,

\* Corresponding author.

\*\* Corresponding author.

E-mail addresses: [jqhuang@bit.edu.cn](mailto:jquang@bit.edu.cn) (J.-Q. Huang), [zhang-qiang@mails.tsinghua.edu.cn](mailto:zhang-qiang@mails.tsinghua.edu.cn) (Q. Zhang).

<sup>1</sup> These authors contribute equally.

many investigations have engaged in establishing a high ionic conductive network to reduce the interfacial resistance between the electrode and electrolyte interface and thus, improving kinetic process of sulfur electrochemistry [5,19–23]. Various sulfide-based solid electrolytes (SSE) with excellent ionic conductivity ( $10^{-3}$ – $10^{-2}$  S cm $^{-1}$ ) and flexible deformability, such as Li<sub>3</sub>PS<sub>4</sub> [24,25], Li<sub>7</sub>P<sub>3</sub>S<sub>11</sub> [26–28], Li<sub>10</sub>GeP<sub>2</sub>S<sub>12</sub> (LGPS) [29,30], Li<sub>6</sub>PS<sub>5</sub>X (X = Cl, Br, I) [31–37], and Li<sub>3+3x</sub>P<sub>1-x</sub>Zn<sub>x</sub>S<sub>4-x</sub>O<sub>x</sub> [38], have been synthesized and employed in ASSLSBs [13,20,29,39]. In addition, sulfur cathode preparations by amendatory mechanical ball milling [32,40,41] and bottom-up approach [42,43] have been also introduced to promote the contacts between active material and SSE.

In general, a biconnected ion/electron contact is the precondition for sulfur conversion in an ASSLSB cell. In a working sulfur cathode, the quality of electron transfer has an equally profound influence on the electrochemical evolution of sulfur in comparison to ion migration for high-efficient sulfur conversion. Various conductive carbon skeletons (e.g. carbon nanotubes (CNTs), ketjen black (KB), reduced graphene oxide (rGO), vapor grown carbon fiber (VGCF), three-dimensional (3D) carbon nanofiber (CNF)) have been widely investigated to promote electron transport [40,41,44–48]. Effective electronic channel establishment strategies are also emerging. For instance, the deposition of nano-amorphous sulfur on rGO through a sulfur–amine chemistry method can maintain high electronic conduction. The uniform distribution of the rGO@S nanocomposite promoted subsequent electron/ion transport, generating uniform volume changes during lithiation/delithiation [45]. The in-situ generation of Li<sub>2</sub>S@C nanocomposite through the combustion of lithium metal in CS<sub>2</sub> also demonstrated a tight contact between the active material and carbon to deliver a rapid electronic transport [43]. In addition, due to the insulative nature of elemental sulfur, conductive selenium used as a eutectic accelerator was also doped into S@pPAN system at molecular level to improve the electronic conductivity [49]. Therefore, nano-confinement of active material [45,50], and in-situ generating mixed conductive nanocomposites [42,43,51] are regarded as effective approaches to enhance the contacts between active material and electronic skeleton. Adopting various conductive agents with different micro-/nano-structures and introducing chemical/electrochemical synthetic methods play a critical role in promoting charge transport and thus achieving an enhanced macro-electrochemical performance for a working solid-state Li–S battery [52]. However, solid-solid interface is generally with a form of point-point contact, which is the main origin of high interfacial impedance. Furthermore, the knowledge and

understanding in interfacial electron transport compared with ion transfer on solid-solid-solid triple-phase interfaces is usually overlooked, which is vital for the construction of biconnected ion/electron conductive frameworks.

In this contribution, we probe the interfacial electron transportation through sulfur and CNT conductive hosts. The influence of electron transport on electrochemical performance of ASSLSBs is probed in two types of interfaces: routine point-to-point (CNT/S) and unique surface-to-surface (CNT@S) interfaces between active sulfur and conductive CNT skeleton. In the same situation of ion migration, the CNT@S composite with more intimate electron contacts enables fast electron transport and reduced interfacial charge transfer impedance and therefore, results in improved conversion kinetics. By virtue of better surface-to-surface electron contacts, the ASSLSBs with CNT@S cathode demonstrate a higher sulfur utilization, delivering a high initial discharge capacity of 1138.7 mAh g $^{-1}$  at 0.1 C and a large capacity retention of 87.7% after 200 cycles.

## 2. Results and discussion

Effective electron transfer is a necessary prerequisite for sulfur electrochemical reaction. To strengthen the understanding on the importance of interfacial electron transport, the solid sulfur cathode composites with different electron transfer capabilities are constructed. A co-axial CNT@sulfur composite with surface-to-surface contacts between sulfur and conductive CNTs (denoted as CNT@S) was firstly established to promote smooth electron transport through uniformly coating elemental sulfur on CNT surface using melting heat treatment. While a routine point-to-point contact with high electron transfer impedance prepared by simply grinding process (denoted as CNT/S) was employed as the control sample (Fig. 1). A tight sulfur-carbon contact renders robust triple-phase interfaces during repeated cycling. In contrast, a loose point-to-point contact leads to a poor electron transfer interface and vast sulfur is at risk of losing contacts with electronic skeleton, likely forming “dead sulfur”.

The as-obtained CNT@S owned 3D interconnect electron networks. The slightly thickened CNTs revealed that dense nano-sulfur was uniformly coated onto CNT surface (Fig. 2a, c; Fig. S2). Both sulfur and CNTs were homogeneously dispersed at both macro and micro scales. As a comparison, CNT/S exhibited worse electronic contacts between active material sulfur and conductive CNTs with micron sized sulfur particles and CNT clusters distributed heterogeneously (Fig. 2b, d; Fig. S1).

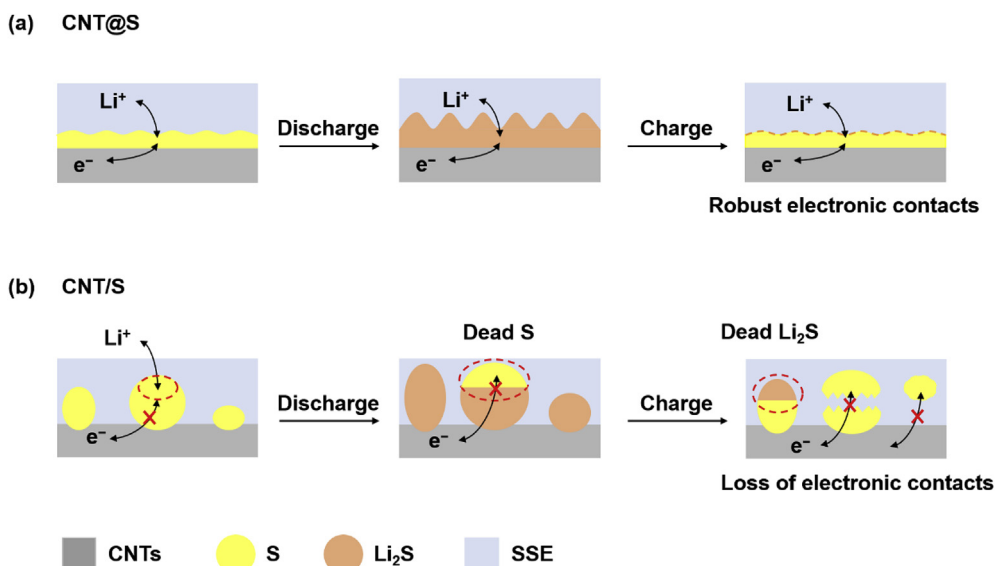
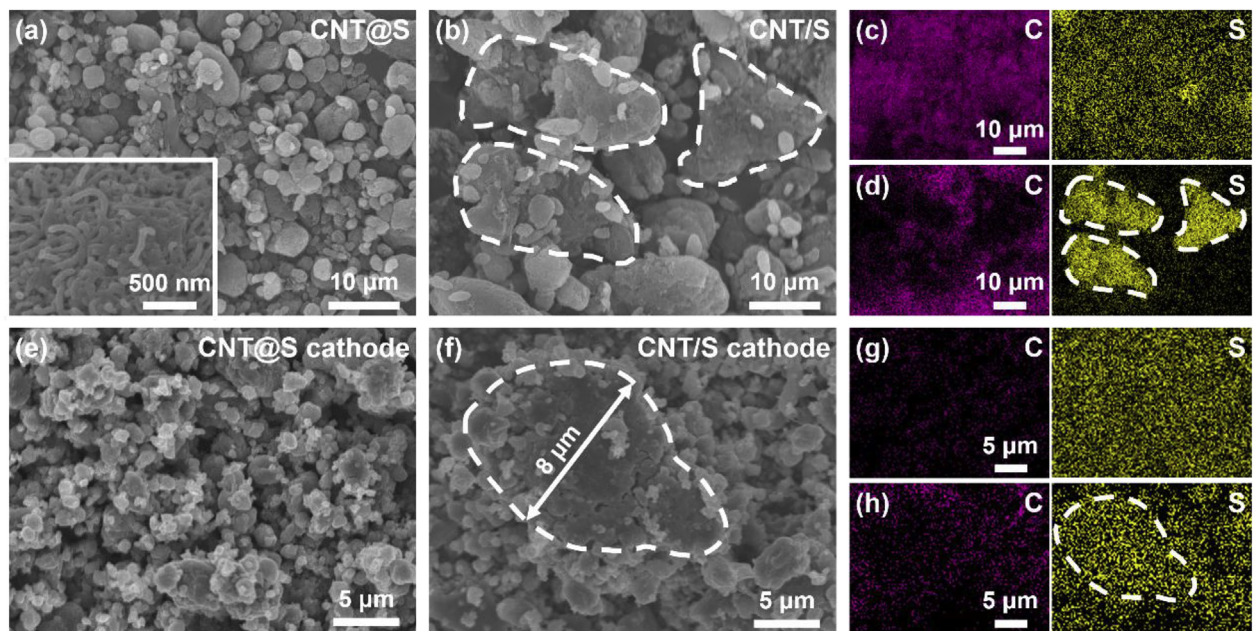


Fig. 1. Schematic illustration of (a) CNT@S with uniform electronic pathway and (b) CNT/S with nonuniform electronic pathway.



**Fig. 2.** SEM images and corresponding EDS elemental mapping images of (a, c) CNT@S, (b, d) CNT/S, (e, g) CNT@S composite cathode, and (f, h) CNT/S composite cathode. The inset of (a) is high resolution image of CNT@S.

Therefore, sulfur in large particles formed “dead sulfur” (Fig. 1b).  $\text{Li}_{10}\text{GeP}_2\text{S}_{12}$  was chosen as an ionic conductor with an actual ionic conductivity of  $\text{ca. } 4.33 \times 10^{-3} \text{ S cm}^{-1}$  in cathode and electrolyte separator (Fig. S3). XRD patterns showed that the crystal structure of cathode

materials did not change after heat treatment and ball milling (Fig. S4). CNT@S composite cathode exhibited a more uniform distribution of C and S element with even particle size around 0.5–2 μm (Fig. 2e, g), while CNT/S composite cathode was much likely to aggregate into larger

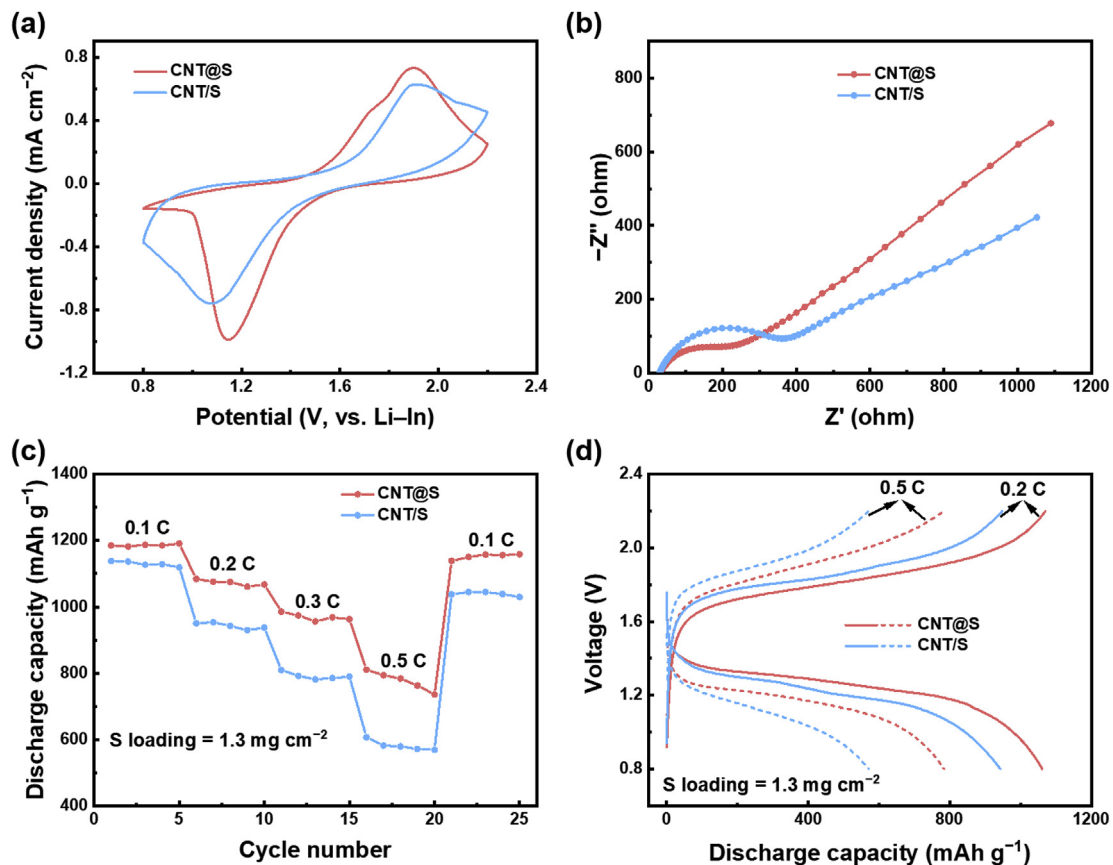


**Fig. 3.** (a) CV curves and (b) EIS curves of Li-In |  $\text{Li}_{10}\text{GeP}_2\text{S}_{12}$  | S all-solid-state cells with different composite cathodes. (c) Rate capacity at a sulfur loading of  $1.3 \text{ mg cm}^{-2}$ . (d) Voltage–capacity curves at different test rates.

particles (about 8  $\mu\text{m}$ ) due to the agglomeration nature of sulfur (Fig. 2f, h; Fig. S7).

To investigate the influence of the enhanced interfacial electron transfer capability on sulfur conversion in ASSLSBs, the reaction kinetics was probed by cyclic voltammogram (CV) measurement using the Li–In |  $\text{Li}_{10}\text{GeP}_2\text{S}_{12}$  | S cell configuration (Fig. 3a). In order to construct a relatively stable anode to inhibit the continuous decomposition of  $\text{Li}_{10}\text{GeP}_2\text{S}_{12}$  on the anode and electrolyte interface, and accurately evaluate the cathode capability, Li–In alloy (ca. 0.6 V vs.  $\text{Li}/\text{Li}^+$ ) was used as the anode [53–57]. The remarkable cathodic and anodic peaks at around 1.1 and 1.9 V demonstrated the solid phase transfer mechanism between S and  $\text{Li}_2\text{S}$ , respectively. Compared to CNT/S composite cathode, CNT@S composite cathode possessed stronger redox peak current and lower polarization, indicating significantly enhanced kinetics. Tafel plots were recorded for further quantitative analysis (Fig. S5). CNT@S cathode delivered a smaller fitting Tafel slopes (230.9 vs. 280.2  $\text{mV dec}^{-1}$  for reduction; 226.1 vs. 378.9  $\text{mV dec}^{-1}$  for oxidation), indicating a faster electron transfer process for the redox reactions of sulfur in CNT@S. Generally, interface impedance is an important index of interface charge transfer barrier. To investigate the enhanced triple-phase interface charge transfer capability, electrochemical impedance spectroscopy (EIS) measurements of ASSLSBs were conducted and corresponding Nyquist plots are shown in Fig. 3b. The bulk resistance of the solid electrolyte ( $R_{SE}$ ) represented by the intercept at high frequency was similar between CNT@S and CNT/S, while CNT@S delivered an obviously reduced interfacial resistance and charge transfer resistance ( $R_{if} + R_{ct}$ ) in the semicircle region [58,59]. EIS results implied that a uniform electronic pathway enabled a lower interfacial impedance and a more rapid charge transfer reaction for Li ion and electron.

To further confirm the impact of promoted electron transfer on facilitating active material sulfur redox chemistry, the electrochemical performance at different charge/discharge rates were evaluated (Fig. 3c).

When increasing current density from 0.1 to 0.2, 0.3, 0.5 C, splendid discharge capacities of 1182.3, 1075.8, 974.2, and 793.9  $\text{mAh g}^{-1}$  for CNT@S were maintained, respectively. In contrast, CNT/S composite cathode displayed a rapid capacity degradation, only exhibiting reversible discharge capacities of 1136.8, 953.7, 791.8, and 581.8  $\text{mAh g}^{-1}$  at 0.1, 0.2, 0.3, and 0.5 C, respectively. Corresponding voltage–capacity profiles further verified the crucial role of rapid electronic transfer. CNT@S composite cathode delivered a lower polarization and higher discharge capacity compared to CNT/S at different test rates (Fig. 3d). Apparently, the outstanding rate capability for CNT@S was ascribed to the superb redox reaction kinetics.

The tight contact capability between electronic skeleton and active material accelerates the electron transfer also facilitates the long-term cycle stability of Li–S full cells (Fig. 4a). The CNT@S composite cathode exhibited an ultrahigh discharge capacity of 1138.7  $\text{mAh g}^{-1}$  at 0.21  $\text{mA cm}^{-2}$  after three cycles of initial activation at a low current density. A stable capacity retention of 87.7% with a reversible capacity of 998.5  $\text{mAh g}^{-1}$  after 200 cycles and a high average Coulombic efficiency of 100.0% were demonstrated. CNT/S composite cathode, in comparison, delivered a discharge capacity of 1052.9  $\text{mAh g}^{-1}$  at 0.21  $\text{mA cm}^{-2}$ , which rapidly faded to 704.4  $\text{mAh g}^{-1}$  after 100 cycles with only 66.9% capacity retention. The sufficient contact between sulfur and CNTs can promote sulfur utilization and thereby, enabling a higher initial discharge capacity. The galvanostatic charge–discharge voltage profiles at 5<sup>th</sup> and 50<sup>th</sup> cycles clearly exhibited the apparent differences in charge and discharge voltage plateaus. The lower voltage gap for CNT@S further verified the faster electrochemical kinetics, which is in good accordance with the lower charge transfer resistance (Fig. 4b).

In order to reveal the dramatically distinguishing capacity retention, conversion efficiency and  $\text{Li}_2\text{S}$  comprehensive utilization were introduced to evaluate the cycle performance. Conversion efficiency is defined as the  $n^{\text{th}}$  charge capacity divided by the  $(n-1)^{\text{th}}$  discharge capacity,

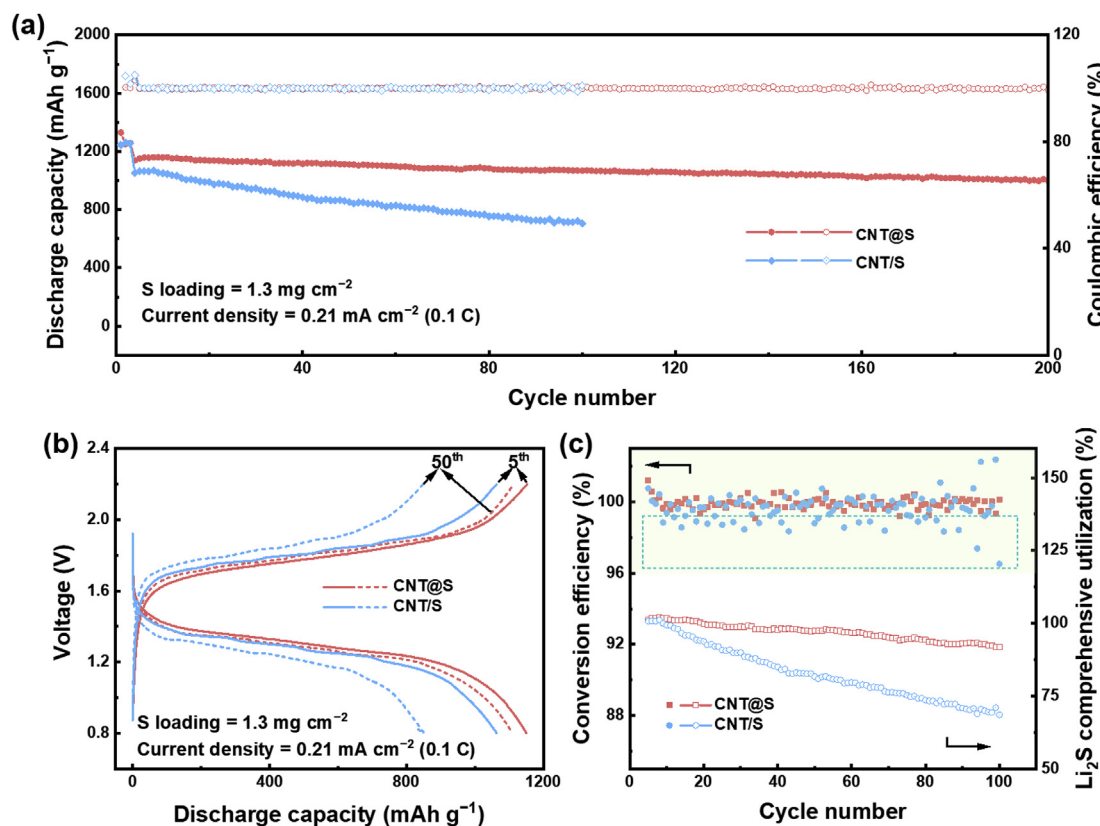


Fig. 4. Electrochemical performance of Li–In |  $\text{Li}_{10}\text{GeP}_2\text{S}_{12}$  | S cells. (a) The cycle lifespan and Coulombic efficiency at sulfur loading of  $1.3 \text{ mg cm}^{-2}$  and  $0.21 \text{ mA cm}^{-2}$  (0.1 C) after three cycles activation at  $0.10 \text{ mA cm}^{-2}$  (0.05 C). (b) Voltage–capacity curves. (c) Conversion efficiency and  $\text{Li}_2\text{S}$  comprehensive utilization for initial 100 cycles.

which describes the conversion capability of  $\text{Li}_2\text{S}$  back to  $\text{S}_8$  [60]. CNT@S composite cathode performed an average conversion efficiency of 99.9% for the initial 100 cycles at  $0.21 \text{ mA cm}^{-2}$ , while that of CNT/S composite cathode was only 99.6% with many discrete points below 99% (Fig. 4c).  $\text{Li}_2\text{S}$  comprehensive utilization was further employed to evaluate the dynamic cumulative utilization of  $\text{Li}_2\text{S}$  where the  $n^{\text{th}}$   $\text{Li}_2\text{S}$  comprehensive utilization is defined as the product of initial  $n$  cycles conversion efficiency. The sharply fading of  $\text{Li}_2\text{S}$  comprehensive utilization for CNT/S cathode implied a severe and continuous active  $\text{Li}_2\text{S}$  loss, while CNT@S cathode exhibited an efficient  $\text{Li}_2\text{S}$  conversion. Actually, if electronic pathway is not established well, the contact between sulfur and CNTs is incompact and insufficient with a sluggish electron transfer. Due to large volume expansion by the transformation of sulfur to  $\text{Li}_2\text{S}$ , carbon skeleton and ionic conductor are much likely to be pushed apart from the active sulfur. While there is a large volume shrinkage when  $\text{Li}_2\text{S}$  is converted back to  $\text{S}_8$  with during reverse process. Therefore, active  $\text{Li}_2\text{S}$  is highly possible to separate from conductive carbon and ionic conductor  $\text{Li}_{10}\text{GeP}_2\text{S}_{12}$  upon repeated charging and discharging. Once  $\text{Li}_2\text{S}$  loses the contact of electronic and ionic conductor, the cell will suffer from lower  $\text{Li}_2\text{S}$  conversion and faster capacity decay. This is corresponding to schematic in Fig. 1.

The influence of effective electron transfer at triple-phase interfaces on active material utilization was further demonstrated through morphology evolution of composite cathodes. After 1<sup>st</sup> discharge, both CNT@S and CNT/S composite cathode shown larger particle size compared to the original cathode before cycle which was because of about 79% volume expansion during conversion from  $\text{S}_8$  to  $\text{Li}_2\text{S}$  (Fig. 5). After 1<sup>st</sup> charge, CNT@S cathode delivered a dramatically smooth and uniform surface without porous structure, while an uneven and coarse surface with random pores and cracks appeared on CNT/S composite cathode. Actually, CNT@S cathode delivered a larger absolute volume shrinkage due to a higher charge capacity (Fig. 4a), which indicated that macro cracks can be avoided even at high absolute volume shrinkage if proper microscale structure design was involved. Sulfur was nano-coated on the CNTs uniformly and tightly in CNT@S, inducing the homogenous volume change. In contrast, uneven space volume variation and generated local stress in CNT/S resulted in local cracking, as a consequence of

which, active material easily separated from electronic framework and caused sluggish kinetics and capacity degradation (Figs. 1b and 4c).

The well-designed electronic network also enables the cycling of Li–S batteries at a high sulfur loading to meet the demand of high-energy density in practical application (Fig. 6). The cell delivered a high initial discharge capacity of  $1330.3 \text{ mAh g}^{-1}$  at  $0.13 \text{ mA cm}^{-2}$  ( $\sim 0.02 \text{ C}$ ) at a sulfur loading of  $3.8 \text{ mg cm}^{-2}$ . The discharge capacity gradually rebounded to  $1249.3 \text{ mAh g}^{-1}$  after 20<sup>th</sup> cycle. With even higher sulfur loading at  $5.9 \text{ mg cm}^{-2}$ , the initial discharge capacity still maintained  $1012.9 \text{ mAh g}^{-1}$  at  $0.10 \text{ mA cm}^{-2}$  ( $\sim 0.01 \text{ C}$ ), and preserved a capacity with  $576.7 \text{ mAh g}^{-1}$  after 20<sup>th</sup> cycle. These results shed fresh light on the rational design of sulfur cathode for ASSLSBs based on fast electron transfer network and efficient sulfur conversion chemistry.

### 3. Conclusions

The vital significance of interfacial electron transport with the rational design of cathode structures was elucidated in Li–S all-solid-state batteries. More intimate contacts between electronic network and active material (CNT@S) enable fast electron transport and reduce interfacial charge transfer impedance, realizing enhanced conversion kinetics. Furthermore, the effective electronic network plays a key role in diminishing the fraction of “dead sulfur”, promoting the active material conversion, and regulating the volume change adaption. Ultimately, rapid redox reaction, low interface impedance, and stable long-term cycle were achieved. ASSLSBs delivered a high initial discharge capacity of  $1138.7 \text{ mAh g}^{-1}$  at  $0.21 \text{ mA cm}^{-2}$  ( $0.1 \text{ C}$ ) with a capacity retention of 87.7% after 200 cycles. This work highlights the role of microstructural electronic pathway regulation in ASSLSBs, and may inspire further rational structure construction of sulfur composite cathode.

### 4. Experimental

#### 4.1. Cathode preparation

Two types of cathode composites were prepared. As for sample CNT@S, sulfur and carbon nanotubes with the weight ratio of 1:1 were

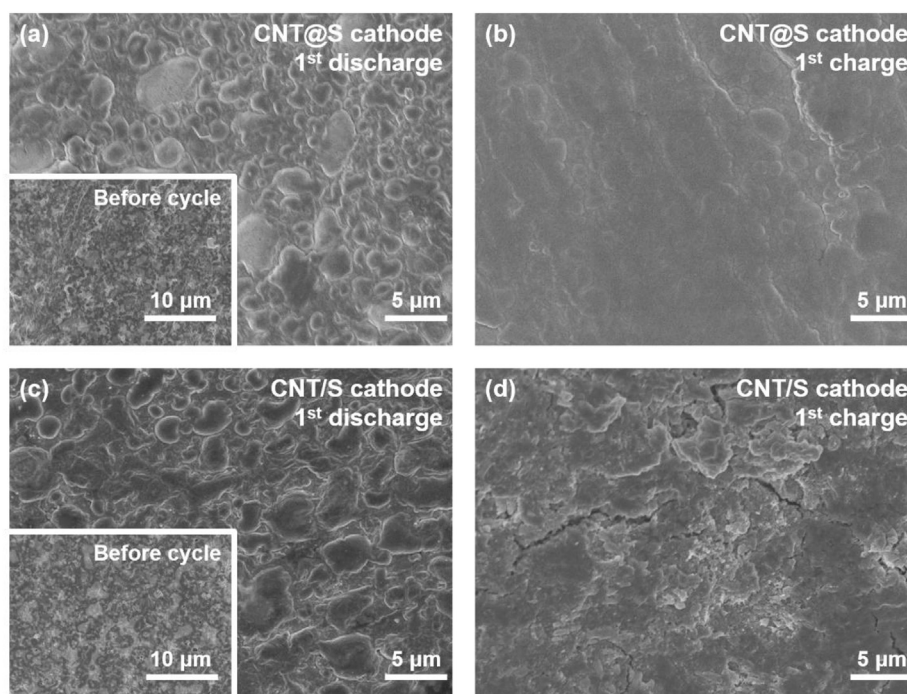


**Fig. 5.** SEM images of CNT@S composite cathode after (a) 1<sup>st</sup> discharge and (b) 1<sup>st</sup> charge. SEM images of CNT/S composite cathode after (c) 1<sup>st</sup> discharge and (d) 1<sup>st</sup> charge. The inset of (a) and (c) is corresponding SEM images of composite cathode before cycle.

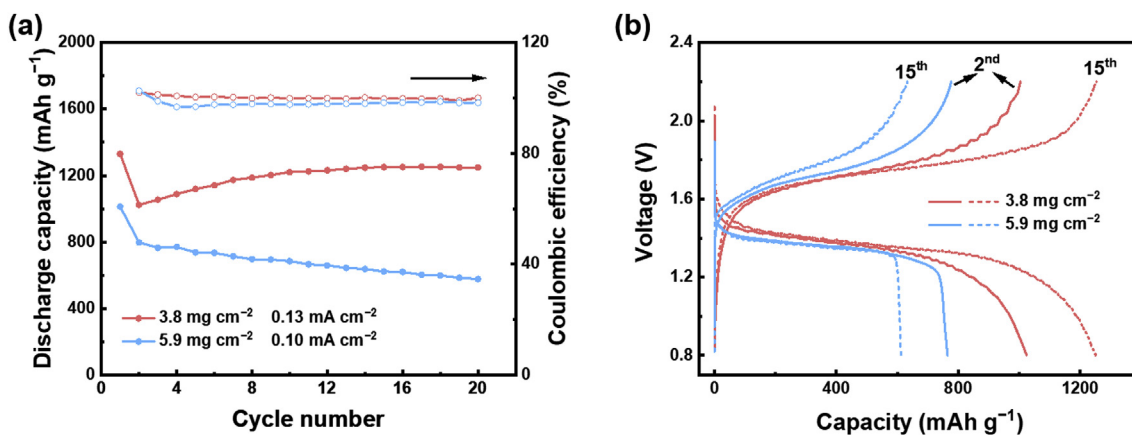


Fig. 6. (a) Electrochemical performance and (b) Voltage–capacity curves of Li–In | Li<sub>10</sub>GeP<sub>2</sub>S<sub>12</sub> | S cells with CNT@S composite cathode at sulfur loading of 3.8 and 5.9 mg cm<sup>-2</sup>.

blended by a planetary mixer with a rotation speed of 2000 rpm for 2 min firstly, and then were sealed in a vessel and heated at 155°C for 3 h. After that, 1.0 g CNT@S composite and 1.0 g Li<sub>10</sub>GeP<sub>2</sub>S<sub>12</sub> (Hefei Kejing Material Technology Co., Ltd.) were mixed and sealed in a 45 mL ZrO<sub>2</sub> ball-milling vessel. 17 milling cycles were conducted, each with 45 min of running at 600 rpm and 15 min rest. The sealing process was in a glove box with oxygen and water contents below 1.0 ppm. The weight ratio of S, CNTs, and Li<sub>10</sub>GeP<sub>2</sub>S<sub>12</sub> in composite cathode was 1:1:2. As a comparison, sulfur and carbon nanotubes were blended by a planetary mixer and then ball-milling with Li<sub>10</sub>GeP<sub>2</sub>S<sub>12</sub> without heat treatment at 155°C. The control was denoted as CNT/S.

#### 4.2. Cell assembly

The cell mold was composed of a poly(ether-ether-ketone) (PEEK) cylinder with an inner diameter of 10 mm. Firstly, 100 mg Li<sub>10</sub>GeP<sub>2</sub>S<sub>12</sub> was pelleted as the solid electrolyte layer under 360 MPa, and then 4.0 mg composite cathode was evenly dispersed on one side of the solid electrolyte under 480 MPa (Fig. S6). The sulfur loading was 1.3 mg cm<sup>-2</sup>. Lithium–indium (Li–In) alloy was employed as anode to ensure a stable interface between the anode and the solid electrolyte. An indium foil with a thickness of 100 μm and a diameter of 10 mm was attached to the opposite side of the electrolyte. And then a lithium foil (Cthina Energy Lithium Co., Ltd) with a thickness of 100 μm and a diameter of 8 mm was pressed on the indium foil under 60 MPa. The whole assemble process was in a glove box with oxygen and water content below 1.0 ppm. As for high loading sulfur cells, the weight of sulfur in composite cathode ranged from 3.0 to 4.6 mg corresponding to sulfur loading from 3.8 to 5.9 mg cm<sup>-2</sup>, respectively.

#### 4.3. Material characterization

Scanning electron microscopy (SEM) images and corresponding elemental energy dispersive X-ray spectroscopy (EDS) were conducted by JSM 7401F (JEOL, Japan). X-ray diffraction (XRD) patterns were acquired by an X-ray powder diffractometer (D8 Advance, Bruker) with a Cu–K<sub>α</sub> radiation source and 2θ in the range of 5°–90° at 5° min<sup>-1</sup>. In order to prevent samples oxidizing by oxygen and water in the atmosphere, Kapton tape was used to cover the samples. Raman spectra was recorded with a He–Ne laser excitation at 532 nm using Horiba Jobin Yvon LabRAM HR800 Raman Spectrometer.

#### 4.4. Electrochemical measurements

Cyclic voltammetry (CV) was performed on Li–In | Li<sub>10</sub>GeP<sub>2</sub>S<sub>12</sub> | S full cells with Solartron electrochemical workstation (1470E). The sweep

rate was 0.1 mV s<sup>-1</sup> with a voltage range from 0.8 V to 2.2 V vs. Li–In alloy. The potential of Li–In alloy is about 0.6 V vs. Li/Li<sup>+</sup>. Electrochemical impedance spectra (EIS) tests were conducted on the same workstation under amplitude of 10 mV at open circuit potential over a frequency range from 10<sup>5</sup> Hz to 0.1 Hz. Galvanostatic charge–discharge cycling tests were performed with LAND multichannel battery cycler (Wuhan LAND Electronics Co., Ltd.). The voltage range was 0.8–2.2 V vs. Li–In alloy, which is equivalent to 1.4–2.8 V vs. Li/Li<sup>+</sup>. The specific capacity was based on the weight of sulfur in cathode (1 C = 1672 mA g<sup>-1</sup>). When the sulfur loading is 1.3 mg cm<sup>-2</sup>, the current density was set at 0.10 mA cm<sup>-2</sup> (~0.05 C) for the first three cycles and 0.21 mA cm<sup>-2</sup> (~0.1 C) for the rest cycles.

#### Acknowledgements

This work was supported by the National Key Research and Development Program (2016YFA0202500 and 2016YFA0200102), National Natural Science Foundation of China (21676160, 21776019, 21825501, 21805162, and U1801257), the Beijing Key Research and Development Plan (Z181100004518001), and the Tsinghua University Initiative Scientific Research Program. We thanks helpful discussion with Li–Da Zhao, Peng Li, and Bo–Chen Zhao.

#### Appendix A. Supplementary data

Supplementary data to this article can be found online at <https://doi.org/10.1016/j.ensm.2019.09.037>.

#### References

- [1] H.-J. Peng, J.-Q. Huang, X.-B. Cheng, Q. Zhang, *Adv. Energy Mater.* 7 (2017) 1700260.
- [2] J. Park, D. Kim, W.A. Appiah, J. Song, K.T. Bae, K.T. Lee, J. Oh, J.Y. Kim, Y.-G. Lee, M.-H. Ryou, Y.M. Lee, *Energy Storage Mater* 19 (2019) 124–129.
- [3] X.Q. Zhang, X.B. Cheng, Q. Zhang, *J. Energy Chem.* 25 (2016) 967–984.
- [4] J. Janek, W.G. Zeier, *Nat. Energy* 1 (2016) 16141.
- [5] Z. Gao, H. Sun, L. Fu, F. Ye, Y. Zhang, W. Luo, Y. Huang, *Adv. Mater.* 30 (2018) 1705702.
- [6] X.-B. Cheng, C.-Z. Zhao, Y.-X. Yao, H. Liu, Q. Zhang, *Chem* 5 (2019) 74–96.
- [7] J. Yue, M. Yan, Y.-X. Yin, Y.-G. Guo, *Adv. Funct. Mater.* 28 (2018) 1707533.
- [8] A. Manthiram, X. Yu, S. Wang, *Nat. Rev. Mater.* 2 (2017) 16103.
- [9] D.N. Lei, K. Shi, H. Ye, Z.P. Wan, Y.Y. Wang, L. Shen, B.H. Li, Q.H. Yang, F.Y. Kang, Y.B. He, *Adv. Funct. Mater.* 28 (2018) 1707570.
- [10] L. Wang, Y. Ye, N. Chen, Y. Huang, L. Li, F. Wu, R. Chen, *Adv. Funct. Mater.* 28 (2018) 1800919.
- [11] T. Ates, M. Keller, J. Kulisch, T. Adermann, S. Passerini, *Energy Storage Mater* 17 (2019) 204–210.
- [12] H. Duan, Y.-X. Yin, X.-X. Zeng, J.-Y. Li, J.-L. Shi, Y. Shi, R. Wen, Y.-G. Guo, L.-J. Wan, *Energy Storage Mater* 10 (2018) 85–91.
- [13] S. Chen, D. Xie, G. Liu, J.P. Mwizerwa, Q. Zhang, Y. Zhao, X. Xu, X. Yao, *Energy Storage Mater* 14 (2018) 58–74.

- [14] C.-Z. Zhao, B.-C. Zhao, C. Yan, X.-Q. Zhang, J.-Q. Huang, Y. Mo, X. Xu, H. Li, Q. Zhang, *Energy Storage Mater* (2020), <https://doi.org/10.1016/j.ensm.2019.07.026>.
- [15] S.P. Culver, R. Koerver, W.G. Zeier, J. Janek, *Adv. Energy Mater.* 9 (2019) 1900626.
- [16] W. Chen, T.Y. Lei, C.Y. Wu, M. Deng, C.H. Gong, K. Hu, Y.C. Ma, L.P. Dai, W.Q. Lv, W.D. He, X.J. Liu, J. Xiong, C.L. Yan, *Adv. Energy Mater.* 8 (2018) 1702348.
- [17] H. Yuan, H.J. Peng, J.Q. Huang, Q. Zhang, *Adv. Mater. Interfaces* 6 (2019) 1802046.
- [18] H. Yuan, H.-J. Peng, B.-Q. Li, J. Xie, L. Kong, M. Zhao, X. Chen, J.-Q. Huang, Q. Zhang, *Adv. Energy Mater.* 9 (2019) 1802768.
- [19] Y. Zhao, K. Zheng, X. Sun, *Joule* 2 (2018) 2583–2604.
- [20] Y.-Z. Sun, J.-Q. Huang, C.-Z. Zhao, Q. Zhang, *Sci. China Chem.* 60 (2017) 1508–1526.
- [21] J. Lau, R.H. DeBlock, D.M. Butts, D.S. Ashby, C.S. Choi, B.S. Dunn, *Adv. Energy Mater.* 8 (2018) 1800933.
- [22] K.H. Park, Q. Bai, D.H. Kim, D.Y. Oh, Y. Zhu, Y. Mo, Y.S. Jung, *Adv. Energy Mater.* 8 (2018) 1800035.
- [23] C. Im, D. Park, H. Kim, J. Lee, *J. Energy Chem.* 27 (2018) 1501–1508.
- [24] Z. Lin, Z. Liu, W. Fu, N.J. Dudney, C. Liang, *Angew. Chem. Int. Ed.* 52 (2013) 7460–7463.
- [25] Z. Liu, W. Fu, E.A. Payzant, X. Yu, Z. Wu, N.J. Dudney, J. Kiggans, K. Hong, A.J. Rondinone, C. Liang, *J. Am. Chem. Soc.* 135 (2013) 975–978.
- [26] J. Liang, X. Li, Y. Zhao, L.V. Goncharova, G. Wang, K.R. Adair, C. Wang, R. Li, Y. Zhu, Y. Qian, L. Zhang, R. Yang, S. Lu, X. Sun, *Adv. Mater.* 30 (2018) 1804684.
- [27] F. Mizuno, A. Hayashi, K. Tadanaga, M. Tatsumisago, *Adv. Mater.* 17 (2005) 918–921.
- [28] Y. Seino, T. Ota, K. Takada, A. Hayashi, M. Tatsumisago, *Energy Environ. Sci.* 7 (2014) 627–631.
- [29] N. Kamaya, K. Homma, Y. Yamakawa, M. Hirayama, R. Kanno, M. Yonemura, T. Kamiyama, Y. Kato, S. Hama, K. Kawamoto, A. Mitsui, *Nat. Mater.* 10 (2011) 682–686.
- [30] K. Suzuki, N. Mashimo, Y. Ikeda, T. Yokoi, M. Hirayama, R. Kanno, *ACS Appl. Energy Mater.* 1 (2018) 2373–2377.
- [31] S. Choi, J. Ann, J. Do, S. Lim, C. Park, D. Shin, *J. Electrochem. Soc.* 166 (2019) A5193–A5200.
- [32] S. Wang, Y. Zhang, X. Zhang, T. Liu, Y.H. Lin, Y. Shen, L. Li, C.W. Nan, *ACS Appl. Mater. Interfaces* 10 (2018) 42279–42285.
- [33] S. Yubuchi, M. Uematsu, M. Deguchi, A. Hayashi, M. Tatsumisago, *ACS Appl. Energy Mater.* 1 (2018) 3622–3629.
- [34] Y. Tian, F. Ding, H. Zhong, C. Liu, Y.-B. He, J. Liu, X. Liu, Q. Xu, *Energy Storage Mater* 14 (2018) 49–57.
- [35] Y.X. Wang, D.P. Lu, J. Xiao, Y. He, G.J. Harvey, C.M. Wang, J.G. Zhang, J. Liu, *Energy Storage Mater* 19 (2019) 80–87.
- [36] F. Han, J. Yue, X. Zhu, C. Wang, *Adv. Energy Mater.* 8 (2018) 1703644.
- [37] Q. Yang, C. Li, *Energy Storage Mater* 14 (2018) 100–117.
- [38] G. Liu, D. Xie, X. Wang, X. Yao, S. Chen, R. Xiao, H. Li, X. Xu, *Energy Storage Mater* 17 (2019) 266–274.
- [39] Y. Kato, S. Hori, T. Saito, K. Suzuki, M. Hirayama, A. Mitsui, M. Yonemura, H. Iba, R. Kanno, *Nat. Energy* 1 (2016) 16030.
- [40] Y. Zhang, T. Liu, Q. Zhang, X. Zhang, S. Wang, X. Wang, L. Li, L.-Z. Fan, C.-W. Nan, Y. Shen, *J. Mater. Chem. A* 6 (2018) 23345–23356.
- [41] M. Nagao, A. Hayashi, M. Tatsumisago, *Electrochim. Acta* 56 (2011) 6055–6059.
- [42] F. Han, J. Yue, X. Fan, T. Gao, C. Luo, Z. Ma, L. Suo, C. Wang, *Nano Lett.* 16 (2016) 4521–4527.
- [43] H. Yan, H. Wang, D. Wang, X. Li, Z. Gong, Y. Yang, *Nano Lett.* 19 (2019) 3280–3287.
- [44] G.-L. Xu, H. Sun, C. Luo, L. Estevez, M. Zhuang, H. Gao, R. Amine, H. Wang, X. Zhang, C.-J. Sun, Y. Liu, Y. Ren, S.M. Heald, C. Wang, Z. Chen, K. Amine, *Adv. Energy Mater.* 9 (2019) 1802235.
- [45] X. Yao, N. Huang, F. Han, Q. Zhang, H. Wan, J.P. Mzwirwa, C. Wang, X. Xu, *Adv. Energy Mater.* 7 (2017) 1602923.
- [46] H. Nagata, Y. Chikusa, *J. Power Sources* 263 (2014) 141–144.
- [47] Q. Zhang, N. Huang, Z. Huang, L. Cai, J. Wu, X. Yao, *J. Energy Chem.* 40 (2020) 151–155.
- [48] P. Zhu, C. Yan, J. Zhu, J. Zang, H. Jia, X. Dong, Z. Du, C. Zhang, N. Wu, M. Dirican, X. Zhang, Y. Li, *Energy Storage Mater* 17 (2019) 220–225.
- [49] Y. Zhang, Y. Sun, L. Peng, J. Yang, H. Jia, Z. Zhang, B. Shan, J. Xie, *Energy Storage Mater* 21 (2019) 287–296.
- [50] Q.G. Han, X.L. Li, X.X. Shi, H.Z. Zhang, D.W. Song, F. Ding, L.Q. Zhang, *J. Mater. Chem. A* 7 (2019) 3895–3902.
- [51] Q. Zhang, H. Wan, G. Liu, Z. Ding, J.P. Mzwirwa, X. Yao, *Nano Energy* 57 (2019) 771–782.
- [52] L. Chen, L.-Z. Fan, *Energy Storage Mater* 15 (2018) 37–45.
- [53] F. Han, Y. Zhu, X. He, Y. Mo, C. Wang, *Adv. Energy Mater.* 6 (2016) 1501590.
- [54] Y. Zhu, X. He, Y. Mo, *ACS Appl. Mater. Interfaces* 7 (2015) 23685–23693.
- [55] K. Takada, N. Aotani, K. Iwamoto, S. Kondo, *Solid State Ion.* 86–88 (1996) 877–882.
- [56] A.L. Santhosha, L. Medenbach, J.R. Buchheim, P. Adelhelm, *Batter. Supercaps* 2 (2019) 524–529.
- [57] M. Nagao, A. Hayashi, M. Tatsumisago, *Electrochemistry* 80 (2012) 734–736.
- [58] R. Koerver, F. Walther, I. Aygün, J. Sann, C. Dietrich, W.G. Zeier, J. Janek, *J. Mater. Chem. A* 5 (2017) 22750–22760.
- [59] R.C. Xu, X.L. Wang, S.Z. Zhang, Y. Xia, X.H. Xia, J.B. Wu, J.P. Tu, *J. Power Sources* 374 (2018) 107–112.
- [60] S. Ohno, R. Koerver, G. Dewald, C. Rosenbach, P. Titscher, D. Steckermeier, A. Kwade, J. Janek, W.G. Zeier, *Chem. Mater.* 31 (2019) 2930–2940.